

MAGNETIC FIELDS IN SHOCKED REGIONS: VERY LARGE ARRAY OBSERVATIONS OF H₂O MASERS

A. P. SARMA,^{1,2} T. H. TROLAND,³ R. M. CRUTCHER,¹ AND D. A. ROBERTS⁴

Received 2002 June 19; accepted 2002 July 30

ABSTRACT

We present VLA observations of the Zeeman effect in 22 GHz H₂O masers in several high-mass star-forming regions. These masers are believed to arise from collisional pumping in postshock environments. Therefore, the Zeeman effect data provide the most direct measurements of magnetic field strengths in high-density ($n \gtrsim 10^8 \text{ cm}^{-3}$) postshock gas, where the field energy determines other physical conditions. Our observations yield significant magnetic field detections in W3 IRS 5, W3(OH), W49 N, and OH 43.8–0.1. In these sources, we detect line-of-sight field strengths ranging from 13 to 49 mG. For some regions, the detected fields provide a 2–3 point sampling of the magnetic field, indicating the nature of field variations on arcsecond scales. These field strengths are consistent with a shock-driven maser model having relatively low speed (20 km s^{-1}), C-type shocks. We examine the balance between magnetic field energy and turbulent kinetic energy in the masing regions. These energies appear close to equilibrium.

Subject headings: ISM: clouds — ISM: magnetic fields — masers — polarization — radio lines: ISM — shock waves

1. INTRODUCTION

Magnetic fields are known to play an important role in the evolution of molecular clouds and star formation (see, e.g., McKee 1999; Heiles et al. 1993). However, the nature of this role is still not fully understood, in part because the observational data on magnetic fields are scarce. The Zeeman effect in radio frequency spectral lines (see, e.g., Crutcher et al. 1993) remains the most direct method for measuring magnetic field strengths. The Zeeman effect in thermally excited H I and OH lines measures magnetic fields in low-density atomic and molecular gas ($n < 10^6 \text{ cm}^{-3}$) in the interstellar medium (see, e.g., Crutcher 1999). The Zeeman effect in 1665 and 1667 MHz OH masers traces magnetic fields in higher density regions up to 10^7 cm^{-3} (see, e.g., Caswell & Reynolds 2001). Even higher density regions ($n \gtrsim 10^8 \text{ cm}^{-3}$) are probed by H₂O masers (see, e.g., Elitzur 1992). Since water is nonparamagnetic, the Zeeman splitting for H₂O masers is very small ($\sim 10^{-3} \text{ Hz } \mu\text{G}^{-1}$, compared to $2.8 \text{ Hz } \mu\text{G}^{-1}$ for H I). Nevertheless, high maser fluxes and narrow line widths make the Zeeman effect in H₂O masers detectable. The first detection was by Fiebig & Güsten (1989), who measured field strengths of $\sim 40 \text{ mG}$ toward several high-mass star-forming regions using the single-dish Effelsberg telescope. Therefore, H₂O masers offer a unique tracer of the Zeeman effect in the highest-density regions. Moreover, H₂O masers are believed to arise in star formation regions as a result of shocks driven by outflows (Elitzur, Hollenbach, & McKee 1989). Since the magnetic field dominates the postshock pressure, an understanding of the physical nature of the shock will be incomplete if the magnetic

field strength is not known. Therefore, water masers are important shock probes, not only for the kinematic information that they reveal, but also because they give information on the magnetic fields in the postshock region.

In this paper, we present VLA observations of the Zeeman effect in H₂O masers toward several star-forming regions. The observations and data reduction are described in § 2. The analysis involved in extracting magnetic field information from the Zeeman effect in H₂O masers is presented in § 3. The results of the VLA observations are given in § 4 and discussed in § 5. The conclusions are given in § 6.

2. OBSERVATIONS AND DATA REDUCTION

The 22 GHz observations of H₂O masers reported in this paper were carried out with the Very Large Array (VLA) of the NRAO⁵ in the A configuration on 1998 May 11 and 1999 July 29. The parameters of the observations are listed in Tables 1, 2, and 3. Both right and left circular polarizations were observed simultaneously. In order to mitigate instrumental effects, a front-end transfer switch in each antenna was used to exchange the postreceiver electronics for the right and left circular polarizations every ~ 10 minutes.

The editing, calibration, imaging, and deconvolution of the data were carried out using the Astronomical Image Processing System (AIPS) of the NRAO. The absolute flux densities were determined with reference to 3C 286. All phase calibrators were observed at the same velocity as the sources; a different phase calibrator was used for each source. A list of the observed sources and phase calibrators is given in Table 2. No bandpass correction was done; bandpass effects usually cancel to first order in Stokes V , and the masers observed for the Zeeman effect are so intense ($I_0 > 100 \text{ Jy}$ for all cases; see Tables 4 and 5) that bandpass corrections will not introduce any appreciable changes.

⁵ The VLA is a facility of the National Radio Astronomy Observatory (NRAO). The NRAO is a facility of the National Science Foundation, operated under cooperative agreement by Associated Universities, Inc.

¹ National Center for Supercomputing Applications and Astronomy Department, University of Illinois at Urbana-Champaign, 1002 West Green Street, Urbana IL 61801; crutcher@astro.uiuc.edu.

² Current address: Physics and Astronomy Department, Eastern Kentucky University, 521 Lancaster Avenue, Richmond, KY 40475; anuj.sarma@eku.edu.

³ Physics and Astronomy Department, University of Kentucky, Lexington, KY 40506; troland@pa.uky.edu.

⁴ Information Technology Division, Northwestern University, Evanston, IL 60208.

TABLE 1
VLA OBSERVATIONAL PARAMETERS FOR H₂O MASERS

PARAMETER	VALUE	
	1998	1999
Date.....	1998 May 11	1999 Jul 29
Configuration	A	A
Rest frequency (MHz).....	22235.08	22235.08
Total bandwidth (MHz).....	0.78	0.78
Velocity range covered (km s ⁻¹)	10.5	10.5
Channels.....	128	128
Hanning smoothing?.....	Yes	Yes
Channel spacing (km s ⁻¹).....	0.08	0.08

We performed the phase calibration for these data in several steps. First, the solutions for the phase calibrators were applied to the sources to derive a “zeroth-order” calibration. The multisource data were then split into individual data sets, each data set containing a single source. For each of these sources, a representative frequency channel containing strong maser emission was selected. Self-calibration was then performed on this channel. For all sources, the first iteration was always a phase self-calibration, under the assumption that the strongest maser was the only source present in that channel. After applying the self-calibration solutions to the UV data in the selected frequency channel, we re-imaged the data and identified clean components in the image, including clean components from masers other than the strongest maser. We then performed several similar phase self-calibration iterations. Finally, solutions for both amplitudes and phases were generated in the last iteration or two of self-calibration. The self-calibration solutions generated for this channel were then applied to all the other channels of that source. The data were then imaged and cleaned. Further processing of the data, including magnetic field estimates, was done with the MIRIAD software. The Gaussian fits to the maser profiles were calculated using the GIPSY task XGAUPROF.

3. ANALYSIS

For cases in which the Zeeman splitting $\Delta\nu_Z$ is much smaller than the line width $\Delta\nu$, the magnetic field can be

obtained from the Stokes V spectrum, which exhibits a *scaled derivative* of the Stokes I spectrum (Heiles et al. 1993). Here, $I = \text{RCP} + \text{LCP}$, and $V = \text{RCP} - \text{LCP}$; RCP is right and LCP is left circular polarization incident on the antennas, where RCP has the standard radio definition of clockwise rotation of the electric vector when viewed along the direction of wave propagation. Moreover, the observed V spectrum might also contain a scaled replica of the I spectrum itself. Thus, the Zeeman effect can be measured by fitting the Stokes V spectra in the least-squares sense to the equation

$$V = aI + \frac{b}{2} \frac{dI}{d\nu} \quad (1)$$

(Troland & Heiles 1982; Sault et al. 1990). The fit parameter a represents the scaled-down replica of the I profile in the V profile; a might result from small calibration errors in RCP versus LCP. Alternatively, a might result from details of the maser emission process described by Nedoluha & Watson (1992). The fit parameter b amounts to the difference in first moments of the line profiles (i.e., the frequency offset) in RCP versus LCP. For thermally excited (nonmaser) lines, $b = zB \cos \theta$, where z is the Zeeman splitting factor, B is the magnetic field, and θ is the angle of the magnetic field to the line of sight (Crutcher et al. 1993). The situation is more complex for H₂O masers, in which the 22 GHz H₂O maser emission can arise from one or more of six closely spaced hyperfine components of the $6_{16}-5_{23}$ rotational transition. Each hyperfine component has a different splitting factor z , with values ranging over an order of magnitude. Also, the relationship between the observed Zeeman splitting and the magnetic field strength might be different for masers than for thermally excited lines, as discussed below.

Nedoluha & Watson (1992) and Elitzur (1996, 1998) have considered theoretically the Zeeman effect in masers. Nedoluha & Watson (1992) solve numerically the equations of radiative transfer and the rate equations for H₂O masers specifically. They find that the thermal equation $b = zB \cos \theta$ is accurate to within a factor of 2 for H₂O masers, as long as the maser line widths are $\lesssim 0.8 \text{ km s}^{-1}$ (also see Watson & Wyld 2001). Line widths discussed here meet this criterion in almost all cases (see Tables 4 and 5). In effect, this result means that the observed Zeeman splitting of H₂O masers is a measure of the line-of-sight field compo-

TABLE 2
INDIVIDUAL H₂O MASER OBSERVATIONAL PARAMETERS

SOURCE	v_{LSR}^a (km s ⁻¹)	POINTING CENTER		TIME ^b (minutes)	PHASE CALIBRATOR
		R.A.	Decl.		
W3 IRS 5	-40.0	02 21 53.3	61 52 21.5	95	0224+671
W3(OH).....	-50.0	02 23 17.5	61 38 57.0	29	0224+671
W49 N ^c	0.0	19 07 49.8	09 01 15.7	26	1923+210
Sgr B2 S	67.0	17 44 10.6	-28 22 39.0	59	1622-297
Cep A.....	-10.0	22 54 19.0	61 45 44.0	58	2320+506
OH 43.8-0.1	37.0	19 09 31.0	09 30 46.0	50	1923+210

NOTE.—Units of right ascension are hours, minutes, and seconds; units of declination are degrees, arcminutes, and arcseconds. For all coordinates stated, including phase calibrator designations, the epoch is B1950.0.

^a Velocity at the center of the observing band.

^b Total time spent on source, not including the time spent on calibrators.

^c W49 N was also observed with v_{LSR} centered at 7.5, -54.0, -67.0, and -73.5 km s⁻¹ for ~25 minutes each, with the same pointing center.

TABLE 3
INDIVIDUAL H₂O MASER IMAGING PARAMETERS

Source	Beam FWHM (arcsec)	Beam P.A. (deg)	rms Noise (mJy beam ⁻¹)
W3 IRS 5	0.11 × 0.09	32.7	20
W3(OH).....	0.10 × 0.09	-16.3	40
W49 N	0.11 × 0.09	20.4	35
Sgr B2 S	0.21 × 0.13	-1.7	80
Cep A.....	0.13 × 0.09	60.7	50
OH 43.8-0.1.....	0.12 × 0.09	30.7	40

nent $B_{\text{los}} (= B \cos \theta)$. Also, under the assumption that the H₂O maser features are principally a blend of the three strongest hyperfine components (Nedoluha & Watson 1991), Nedoluha & Watson (1992) find an effective value of $z = 2.1 \text{ Hz mG}^{-1}$ for H₂O masers. Elitzur (1996, 1998) considered the more general case of the polarization of astronomical masers, adopting a purely analytic approach. He finds a quite different relation between the fit parameter b and the magnetic field. For a saturated maser, he finds $b = 8zB/3p \cos \theta$ (we use $zB/2$ in place of his $\Delta\nu_B$), where p represents the dimensionality of the maser: $p = 1$ for filamentary, 2 for planar, and 3 for spherical masers, respectively. In the Elitzur (1998) formulation, the observed Zeeman splitting is not a measure of B_{los} ; rather, it is a measure of $B/\cos \theta$. M. Elitzur (2002, private communication) also states that the dimensionality parameter p belongs in the thermal equation if it is applied to maser radiation, i.e., $b = (zB \cos \theta)/p$. Therefore, the Elitzur result implies that magnetic field strengths derived with the thermal assumption are too high by a factor of $8/(3 \cos^2 \theta)$. This factor amounts to 5.3 for $\theta = 45^\circ$, and it becomes an order of magnitude for $\theta = 60^\circ$. However, Elitzur's general treatment of maser polarization did not include the effects of hyperfine splitting. Hence, the Elitzur predictions above might not be directly applicable to the observations of the Zeeman effect in H₂O masers.

4. RESULTS

4.1. W3 IRS 5

The W3 giant molecular cloud (GMC) is located in the Perseus arm at a distance of $\sim 2 \text{ kpc}$ (Georgelin & Georgelin 1976; Imai et al. 2000). W3 Main is one of the sites of ongoing star formation in this GMC. W3 IRS 5 is an infrared double source in W3 Main, located between the H II regions W3 A and W3 B at $\alpha_{1950} = 02^{\text{h}}21^{\text{m}}53^{\text{s}}.2$, $\delta_{1950} = 61^\circ 52' 21''$ (Wynn-Williams, Becklin, & Neugebauer 1972). Claussen et al. (1994) found seven hypercompact radio continuum sources in the W3 IRS 5 region with the VLA; these sources have diameters less than 700 AU (Tieftrunk et al. 1997). The hypercompact sources are candidates for newly formed high-mass stars. Strong H₂O masers appear in the vicinity of these hypercompact continuum sources. Imai et al. (2000) measured the proper motions of the water masers in W3 IRS 5 with the Very Long Baseline Array (VLBA), and they found that the masers can be divided into two groups; these two groups might be associated with two different outflows (also see Imai, Deguchi, & Sasao 2002). Both outflows are aligned approximately north-south; their directions are not significantly different from the direction of the global outflow seen in CO ($J = 2-1$) emission (Claussen et al. 1984). The outflows originate near two of the hypercompact continuum sources; Imai et al. (2000) conclude that these hypercompact features might be the driving sources of the outflows.

The results of the VLA observations for W3 IRS 5 are given in Table 4. Since the rms in $V/2$ is 20 mJy (see Table 3) and $V/I \sim 10^{-3}$ for H₂O masers, the Zeeman effect in the W3 IRS 5 data can be detected at the 3σ level if $I_0 > 120 \text{ Jy}$. The locations of the peak maser near -40 km s^{-1} and two neighboring maser sources that satisfy this criterion are shown in Figure 1. There is no other observed maser source with $I_0 > 120 \text{ Jy}$ in the region displayed in this figure. The sources at (0, 0) and (0''13, 0''15) in Figure 1 each have one prominent velocity component. Significant detections of the Zeeman effect have been made in both these sources. We consider the detections to be significant only if the fits of V

TABLE 4
H₂O MASER PARAMETERS AND MAGNETIC FIELD DETECTIONS

MASER	POSITION		v_{LSR} (km s ⁻¹)	Δv_{FWHM} (km s ⁻¹)	AMPLITUDE I_0 (Jy)	FIT OUTPUT b^a (Hz)	B_{los}^a (mG)
	$\Delta\alpha$ (arcsec)	$\Delta\delta$ (arcsec)					
W3 IRS 5	0	0	-40.0	0.58	432.7 ± 1.1	-39.1 ± 2.7	-18.6 ± 1.3
	0.13	0.15	-40.2	0.45	332.7 ± 0.3	-27.1 ± 2.8	-12.9 ± 1.3
	0.10	0.40	-41.2	0.75	557.2 ± 3.0	-103.2 ± 10.2	-49.1 ± 4.9
W3(OH).....	0	0	-49.1	0.67	3795.7 ± 3.8	+88.5 ± 6.5	+42.1 ± 3.1
W49 N	0.38	0.25	-3.3	0.66	595.4 ± 6.7	-48.1 ± 2.7	-22.9 ± 1.3
OH 43.8-0.1.....	-0.70	0.50	-0.71	0.75	851.0 ± 4.5	+34.8 ± 3.9	+16.6 ± 1.9
	0	0	36.5	0.79	1133.9 ± 4.5	-40.3 ± 3.4	-19.2 ± 1.6
	38.1	0.54	1087.7 ± 5.4	-96.9 ± 5.3	-46.1 ± 2.5
	40.1	0.42	668.6 ± 6.0	-27.9 ± 2.9	-13.3 ± 1.4

NOTES.—Quantity b is the result of the Zeeman fits (eq. [1]). The reference feature (0, 0) for W3 IRS 5 is $\alpha_{1950} = 02^{\text{h}}21^{\text{m}}53^{\text{s}}.24$, $\delta_{1950} = 61^\circ 52' 21''.1$. For W3(OH), the (0, 0) position is $\alpha_{1950} = 02^{\text{h}}23^{\text{m}}17^{\text{s}}.48$, $\delta_{1950} = 61^\circ 38' 57''.4$. For W49 N (0, 0) is $\alpha_{1950} = 19^{\text{h}}07^{\text{m}}49^{\text{s}}.81$, $\delta_{1950} = 09^\circ 01' 15''.1$, and for OH 43.8-0.1, it is $\alpha_{1950} = 19^{\text{h}}09^{\text{m}}30^{\text{s}}.92$, $\delta_{1950} = 09^\circ 30' 46''.3$. In all cases, errors in positions are $\leq 0''.1$, except for W3(OH), for which the positional error is $\leq 0''.2$. The line parameters have been derived from Gaussian fits; errors in v_{LSR} and Δv are $\leq 0.01 \text{ km s}^{-1}$.

^a Values given are the results of the fit $\pm 1 \sigma$ error; all stated values of b and B_{los} are significant detections (at 3σ). Values for B_{los} have been obtained from the Zeeman equation for thermally excited lines, using $z = 2.1 \text{ Hz mG}^{-1}$ (Nedoluha & Watson 1992; also see § 3).

TABLE 5
MAGNETIC FIELD UPPER LIMITS

MASER	POSITION		v_{LSR} (km s ⁻¹)	Δv_{FWHM} (km s ⁻¹)	AMPLITUDE I_0 (Jy)	FIT OUTPUT b^a (Hz)	B_{los}^a (mG)
	$\Delta\alpha$ (arcsec)	$\Delta\delta$ (arcsec)					
Sgr B2 S	0	0	66.1	0.71	1164 ± 5	-16.0 ± 6.1	-7.6 ± 2.9
Cep A.....	-1.39	+2.55	-8.8	0.70	2494 ± 9	-6.7 ± 3.3	-3.2 ± 1.6
W49 N	0	0	-72.7	1.12	6967 ± 24	-155.6 ± 10.1^b	-74.1 ± 4.8^b
...	-71.1	1.06	4085 ± 25	-98.5 ± 19.6^b	-46.9 ± 9.3^b

NOTES.—Quantity b is the result of the Zeeman fits (eq. [1]). The reference feature (0, 0) for Cep A is $\alpha_{1950} = 22^{\text{h}}54^{\text{m}}19^{\text{s}}.24$, $\delta_{1950} = 61^{\circ}45'44''.1$, and for W49 N it is $\alpha_{1950} = 19^{\text{h}}07^{\text{m}}49^{\text{s}}.77$, $\delta_{1950} = 09^{\circ}01'15''.6$. In both cases, errors in positions are $<0''.1$. For Sgr B2 S, the zeroth-order phase calibrations applied from 1622–297 failed to give a good fix on position. Hence, there is no absolute position information for this source. The (0, 0) position is for the strongest maser at $v_{\text{LSR}} = 66.1$ km s⁻¹. The pointing center for Sgr B2 S is given in Table 2. The line parameters have been derived from Gaussian fits; errors in v_{LSR} and Δv are ≤ 0.01 km s⁻¹.

^a Values given are the results of the fit $\pm 1 \sigma$ error; all stated values of b and B_{los} in this table are upper limits. Values for B_{los} have been obtained from the Zeeman equation for thermally excited lines, using $z = 2.1$ Hz mG⁻¹ (Nedoluha & Watson 1992; also see § 3).

^b Although formally significant, the results for W49 N (observations centered at -73.5 km s⁻¹) have been stated as upper limits because of blending in velocity.

to I (eq. [1]) are above the 3σ level. Table 4 gives the positions and line parameters for these two maser sources, together with the Zeeman effect results. Values are provided for the derived Zeeman splittings b (eq. [1]; for all H₂O masers discussed in this paper, the value of a in this equation is $\sim 10^{-3}$ or less). Values are also provided for the line-of-sight magnetic field B_{los} , using the results of Nedoluha & Watson

(1992), i.e., using the thermal assumption with $z = 2.1$ Hz mG⁻¹ (§ 3). By convention, a negative value for B_{los} indicates a field pointing toward the observer. Figure 2 shows the Stokes I and V profiles for the -40 km s⁻¹ maser at posi-

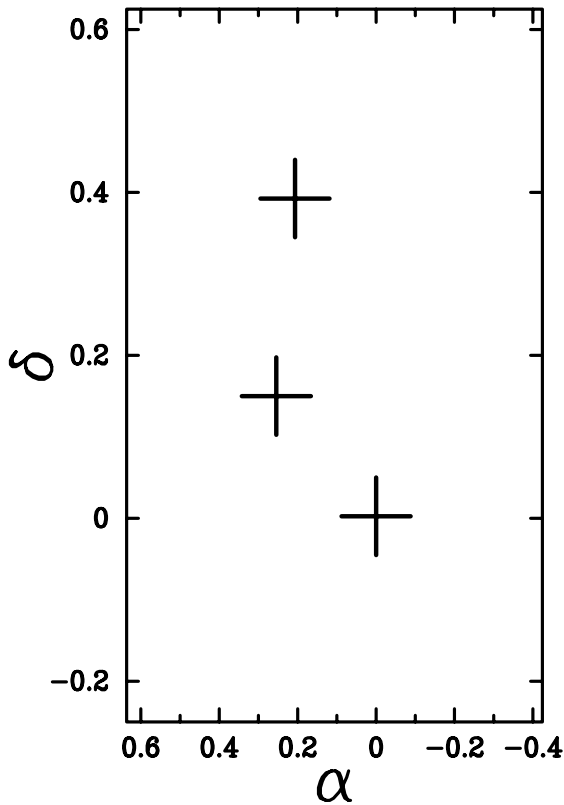


FIG. 1.—Image of a $0''.5 \times 0''.9$ region around the peak maser near -40 km s⁻¹ in W3 IRS 5. The two other masers with intensity $I_0 > 120$ Jy are also marked. The (0, 0) position is $\alpha_{1950} = 02^{\text{h}}21^{\text{m}}53^{\text{s}}.24$, $\delta_{1950} = 61^{\circ}52'21''.1$. The α -axis should be multiplied by $\cos \delta_{1950} = 0.47$, in order to get the value in absolute arcseconds (the values for the maser positions are given in Table 4); the δ -axis is in arcseconds.

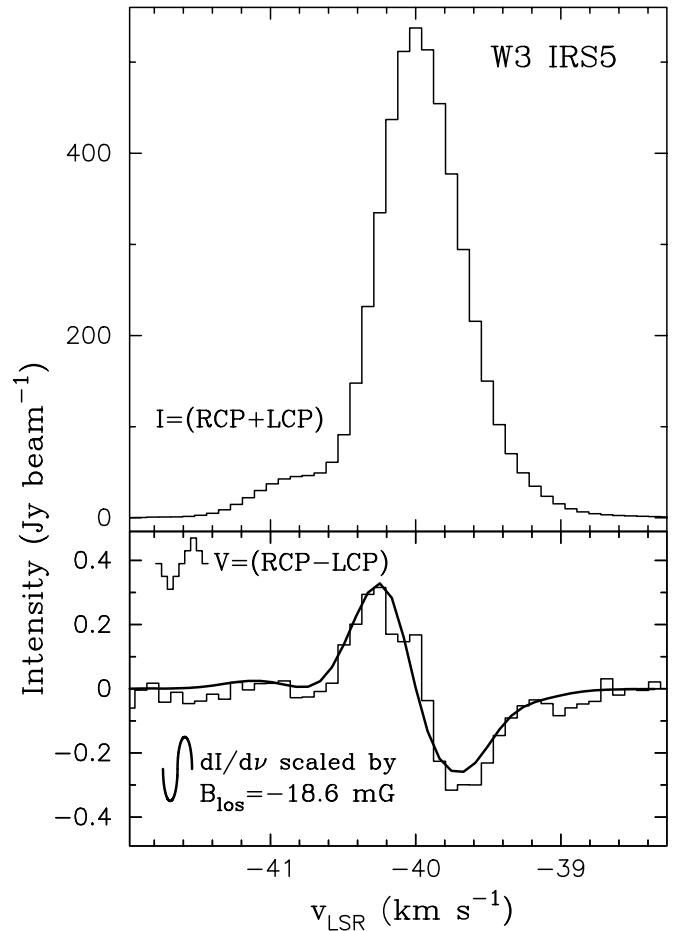


FIG. 2.—Stokes I (top) and V (bottom) profiles of the -40 km s⁻¹ maser in W3 IRS 5 at the position (0, 0) in Fig. 1 (histograms). The superposed curve in the bottom panel shows the derivative of I scaled by $B_{\text{los}} = -18.6 \pm 1.3$ mG. The V profile is that obtained after leakage correction, i.e., $V - aI$, as described in § 3 (eq. [1]).

tion (0, 0) in Figure 1, together with the derivative of I scaled by the derived value of B_{los} and superposed on the V profile. All V profiles displayed are those obtained after removal of the scaled-down I profile, i.e., $V - aI$, as described in § 3 (see eq. [1]).

The third and northernmost maser source shown in Figure 1 (0''10, 0''40) exhibits four velocity components. Only one of these velocity components displays the Zeeman effect with certainty. For this component at $v_{\text{LSR}} = -41.2 \text{ km s}^{-1}$, $b = -103 \pm 10 \text{ Hz}$ ($B_{\text{los}} = -49 \pm 5 \text{ mG}$). A second velocity component toward this source ($v_{\text{LSR}} = -42.5 \text{ km s}^{-1}$, $\Delta v = 0.76 \text{ km s}^{-1}$, and $I_0 = 839 \text{ Jy}$) also shows some indication of a Zeeman pattern, with $b = -133 \pm 38 \text{ Hz}$ ($B_{\text{los}} = -64 \pm 18 \text{ mG}$), barely above the 3σ limit. Therefore, this result has not been included in Table 4. However, these two results are equal to within the errors.

The absolute positions of the W3 IRS 5 H_2O masers are slightly uncertain, with earlier determinations by Forster, Welch, & Wright (1977) likely to have small errors. Positions reported by these authors were derived with a two-element interferometer at Hat Creek. They were later used as a reference for the VLBI observations of Genzel et al. (1978). Forster et al. (1977) located three masers in a cluster centered near $\alpha_{1950} = 02^{\text{h}}21^{\text{m}}53^{\text{s}}.15$, $\delta_{1950} = 61^{\circ}52'22''.0$. This position is offset approximately $0''.1$ to the west and $0''.8$ to the north of our reference position, shown in Figure 1. We estimate that errors in our absolute positions are $\leq 0''.1$. Forster et al. (1977) report comparable formal errors. Therefore, the two sets of positional determinations are inconsistent. Dreher & Welch (1981) used the VLA to determine absolute positional information for the H_2O masers in the W3(OH) region (see § 4.2 below). They inferred a positional offset relative to Forster et al. (1977) that is very comparable to the offset (between our data and the Forster et al. 1977 data) given above. Therefore, we conclude that our positional information for the W3 IRS 5 source is likely to be more reliable than that of Forster et al. (1977).

4.2. W3(OH)

The W3(OH) region lies $\sim 15'$ southeast of W3 Main (see § 4.1). Strong OH maser emission is observed in this region (Reid et al. 1980), associated with a shell-like, ultracompact (UC) H II region of diameter $2''.5$ (Dreher & Welch 1981). The H_2O masers in this region are located $\sim 6''$ east of this UC H II region ($\equiv 0.06 \text{ pc}$ at 2.3 kpc ; Humphreys 1978). This group of H_2O masers is also referred to as W3(H_2O) in the literature. It appears to be the site of the most recent high-mass star formation. Embedded in W3(H_2O) is a warm, high-density, compact molecular clump first detected in HCN emission (Turner & Welch 1984). Proper motions of the H_2O masers have been interpreted as evidence of a bipolar outflow centered on this Turner-Welch object (Alcolea et al. 1993). Nonthermal continuum emission has also been detected in this region (Reid et al. 1995). This nonthermal continuum source is coincident with the center of expansion of the H_2O maser outflow. It is also elongated in the east-west direction; thus, it is aligned with the dominant H_2O maser outflow pattern. Wyrowski et al. (1997) observed compact continuum emission from hot dust (112 and 225 GHz) toward the cluster of H_2O masers. They also observed the region in the $J = 1-0$ and $J = 2-1$ lines of C^{17}O . Their C^{17}O images show gas that is more extended than the dust continuum, with the most massive molecular clump toward

the cluster of H_2O masers; no C^{17}O emission is observed toward the UC H II region itself.

Our only detection of the Zeeman effect in this region is in the strongest maser, centered at -49.1 km s^{-1} in velocity and located at $\alpha_{1950} = 02^{\text{h}}23^{\text{m}}17^{\text{s}}.48$, $\delta_{1950} = 61^{\circ}38'57''.4$. The uncertainty in the position is $\leq 0''.2$. This position places the maser near the -48.1 km s^{-1} maser in the Dreher & Welch (1981) data. A slight asymmetry in the line profile of the -49.1 km s^{-1} maser from the current observations leads one to suspect that there must be two masers closely spaced in velocity. Indeed, Gaussian fits to this maser profile required more than one component. The parameters of the primary component are listed in Table 4. A second component was centered at $v_{\text{LSR}} = -48.58 \text{ km s}^{-1}$, with $\Delta v = 0.63 \text{ km s}^{-1}$ and amplitude $I_0 = 1425 \text{ Jy}$. A third broad component at $v_{\text{LSR}} = -48.62 \text{ km s}^{-1}$, $\Delta v = 1.9 \text{ km s}^{-1}$, and $I_0 = 471 \text{ Jy}$ was also used to fit the lower level wings. The results of the Zeeman fits, b and B_{los} , calculated as described earlier, are given in Table 4. The Stokes I and V profiles, together with the scaled derivative of I , are shown in Figure 3. The fit was performed only over one side of the profile. The result of fitting over the entire profile gives an unsatisfactory result. This is likely due to the blending of the masers in velocity. Higher resolution observations (e.g., with the VLBA) should allow us to resolve this issue satisfactorily.

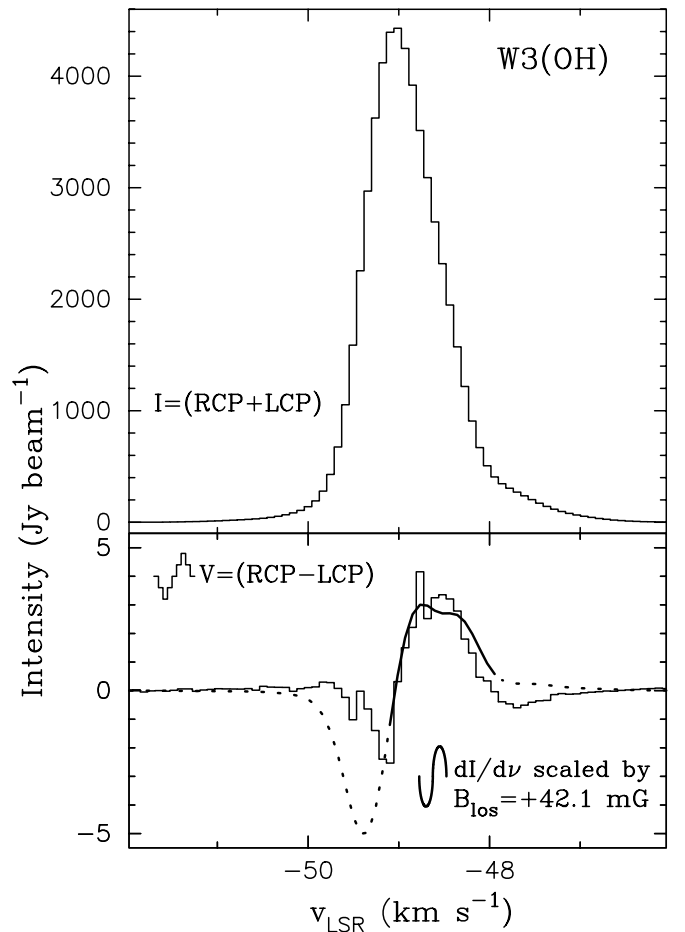


FIG. 3.—Same as Fig. 2, but for the peak maser in W3(OH). The superposed curve in the bottom panel is scaled by $B_{\text{los}} = +42.1 \pm 3.1 \text{ mG}$. The solid portion of this curve represents the channels over which the fit was made.

4.3. W49 N

The radio source W49 is located at a distance of 11.4 kpc (Gwinn, Moran, & Reid 1992). At low resolution, it consists of two radio continuum peaks: a thermal source (W49 A) and a nonthermal source (W49 B) $\sim 12'$ to the east. Low-resolution radio continuum images of the thermal source and star-forming region W49 A show two well-defined peaks: W49 North (W49 N) and W49 South (W49 S). W49 N hosts one of the most complex H_2O maser sources in the Galaxy, with features spread over more than 500 km s^{-1} in velocity (Morris 1976). From VLBI observations, Moran et al. (1973) found that the H_2O maser spots in W49 N are localized in three regions. Walker, Matsakis, & García-Barreto (1982) found a distinct separation of the positive ($v_{\text{LSR}} > 30 \text{ km s}^{-1}$) and negative ($v_{\text{LSR}} < -20 \text{ km s}^{-1}$) high-velocity H_2O maser features in this region using a three-antenna, long-baseline interferometer, with negative high-velocity features occurring predominantly in the westernmost group of masers. In the W49 N core, Dreher et al. (1984) identified seven distinct UC H II regions with the VLA. These UC regions are arranged in a partial ring of diameter 0.8 pc and powered by O stars. De Pree et al. (2000) have imaged W49 N at 1.3 and 0.7 cm. They used the high-resolution 1.3 cm continuum images, made concurrently with 22 GHz H_2O maser observations, to align the maser positions with the high-resolution 0.7 cm continuum. They found that most of the H_2O maser positions in W49 N are closely associated with the sources G1 and G2, which are part of the UC H II source G identified by Dreher et al. (1984). The H_2O masers toward this source trace an outflow (Gwinn et al. 1992); De Pree et al. (2000) find that this outflow is centered within $0''.2$ of the G2 peak, although it remains unclear whether this source drives the outflow.

Because of the limited frequency bandwidth available at the VLA, our H_2O maser observations of W49 N were centered at several different velocities, in order to cover a larger velocity range. The center velocities of 0, 7.5, -54 , -67 , and -73.5 km s^{-1} were selected because of the presence of strong masers at or near these velocities. The total velocity range covered in each of the bands was 10.5 km s^{-1} (Table 1). The pointing center was the same in all the velocity ranges (Table 2). For the observations centered at 0 km s^{-1} , Zeeman effect detections were made in two maser sources. The line parameters and Zeeman results for these sources are given in Table 4. The Stokes I and V profiles for the -0.7 km s^{-1} maser, together with the derivative of I scaled by the fitted value of B_{los} , are shown in Figure 4.

The peak maser in the W49 N observations centered at 0 km s^{-1} (with $v_{\text{LSR}} = 0.5 \text{ km s}^{-1}$, $\Delta v \sim 0.9 \text{ km s}^{-1}$, and $I_0 \sim 2800 \text{ Jy}$) does not display a detectable Zeeman effect. This might be due to blending in velocity; there is at least one other maser at $v_{\text{LSR}} = -0.9 \text{ km s}^{-1}$ ($\Delta v \sim 1.0 \text{ km s}^{-1}$ and $I_0 = 750 \text{ Jy}$) at this position. Likewise, the masers in the observations centered at 7.5, -54 , and -67 km s^{-1} were so heavily blended in velocity that no useful Zeeman information could be obtained from these data. The masers in the -73.5 km s^{-1} data set also display blending in velocity, but we were able to obtain values for the magnetic field in two velocity components toward the peak maser position. Although they are formally significant, we have chosen to state these values as upper limits in Table 5 because of the blending in velocity. Future higher resolution observations with the VLBA will likely

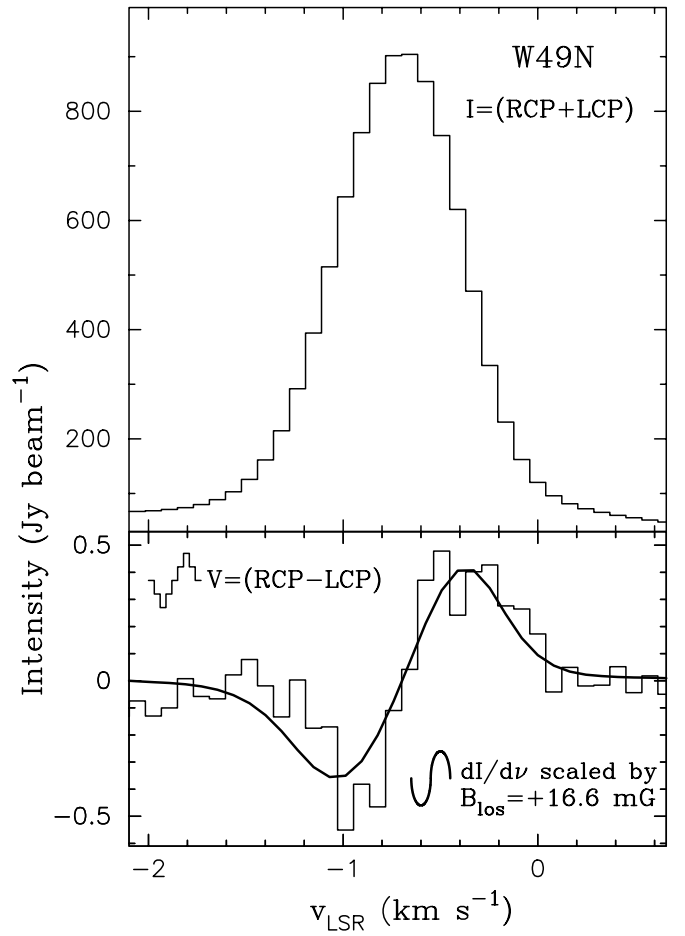


FIG. 4.—Same as Fig. 2, but for the -0.7 km s^{-1} maser in W49 N (see Table 4). The superposed curve in the bottom panel is scaled by $B_{\text{los}} = +16.6 \pm 1.9 \text{ mG}$.

be able to disentangle this blending in velocity by spatially resolving the maser spots.

Of the three groups of masers in W49 N identified by Walker et al. (1982), the maser source at the (0, 0) position in our 0 km s^{-1} data set is located in the central group (the VLA position for this maser is given in the notes to Table 4). Hence, the detected fields in W49 N are for masers belonging to this central concentration of mainly low-velocity masers ($-20 < v_{\text{LSR}} < 30 \text{ km s}^{-1}$). Conversely, the (0, 0) position for the -73.5 km s^{-1} data set in W49 N (see notes to Table 5) places this negative high-velocity maser source in the westernmost group of masers, with $v_{\text{LSR}} < -20 \text{ km s}^{-1}$. We have obtained upper limits for B_{los} toward the -73.5 km s^{-1} maser. Hence, the Zeeman effect data give some sense of magnetic field values in these two main concentrations of H_2O masers. Line-of-sight fields in the central group are $\sim 20 \text{ mG}$, whereas fields in the group of blue-shifted masers to the west are less than 89 mG .

4.4. OH 43.8–0.1

OH 43.8–0.1 is an H_2O maser source associated with a compact H II region and a 1665 MHz OH maser (within a $10''$ positional uncertainty; Matthews et al. 1978; Downes et al. 1979). The most intense H_2O masers in OH 43.8–0.1 are spread over a 5 km s^{-1} range in velocity (low-velocity lines); also present are weaker high-velocity features spread over a

40 km s⁻¹ range (Downes et al. 1979). The VLBI image of Downes et al. (1979) shows that most of the H₂O maser features are arranged in an arc-shaped structure with a transverse diameter of ~ 200 mas. The radial velocities of the strongest low-velocity features increase from east to west along this arc. High-velocity features also occur ~ 400 mas below the open end of the arc. Our VLA observations reveal about four maser sources that are spread over an east-west extent of $0''.3$. This must be a part of the arc observed by Downes et al. (1979) with VLBI. Zeeman effect detections were made in the strongest maser source in OH 43.8–0.1. There are four velocity components at the position of this source; the Zeeman effect was detected in three of these components. The line parameters and results of the Zeeman fits are given in Table 4. Figure 5 shows the Stokes *I* and *V* profiles for the maser at this position, together with the scaled values of the derivative of the *I* profile for fits over the 36.5 and 38.1 km s⁻¹ maser profiles.

4.5. Other Results

4.5.1. Sagittarius B2 S

Sgr B2 is a well-studied active star-forming region ~ 200 pc from the Galactic center. Low-resolution CO observations show that it has a core of $2''$ diameter, surrounded by a

15' envelope (Scoville, Solomon, & Penzias 1975). VLA continuum observations by Benson & Johnston (1984) have revealed at least 12 H II regions in Sgr B2. These are grouped into three main concentrations: the northern, middle, and southern (Sgr B2 S) sources, separated by $\sim 45''$ each. Strong H₂O maser emission is observed near all three groups of H II regions (Elmegreen et al. 1980). The H₂O masers toward the Sgr B2 S source were observed with the VLA for the Zeeman effect (Table 2). Of the three main concentrations of masers, the southern concentration was selected because it has an isolated component in velocity that is also very intense. Only an upper limit could be set on the magnetic field in this source. The line parameters for the strongest maser and the results of the fits for the Zeeman effect are given in Table 5. The obtained formal fit for B_{los} gives a 3σ upper limit field of 17 mG. This value is close to the significant fields detected in most regions (Table 4).

4.5.2. Cepheus A

Cep A is a CO peak (Sargent 1977) in a molecular cloud near the Cepheus OB3 association (distance ~ 725 pc; Blaauw, Hiltner, & Johnson 1959). It contains several UC ($\sim 1''$) H II regions (Rodríguez et al. 1980). Lada et al. (1981) found that the H₂O masers in this complex are clustered in

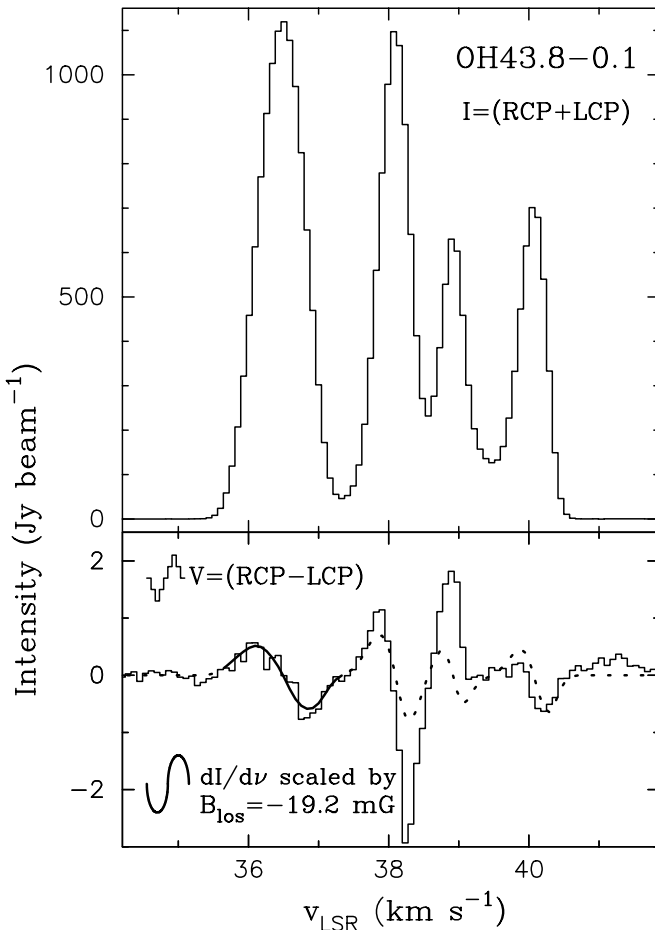


FIG. 5a

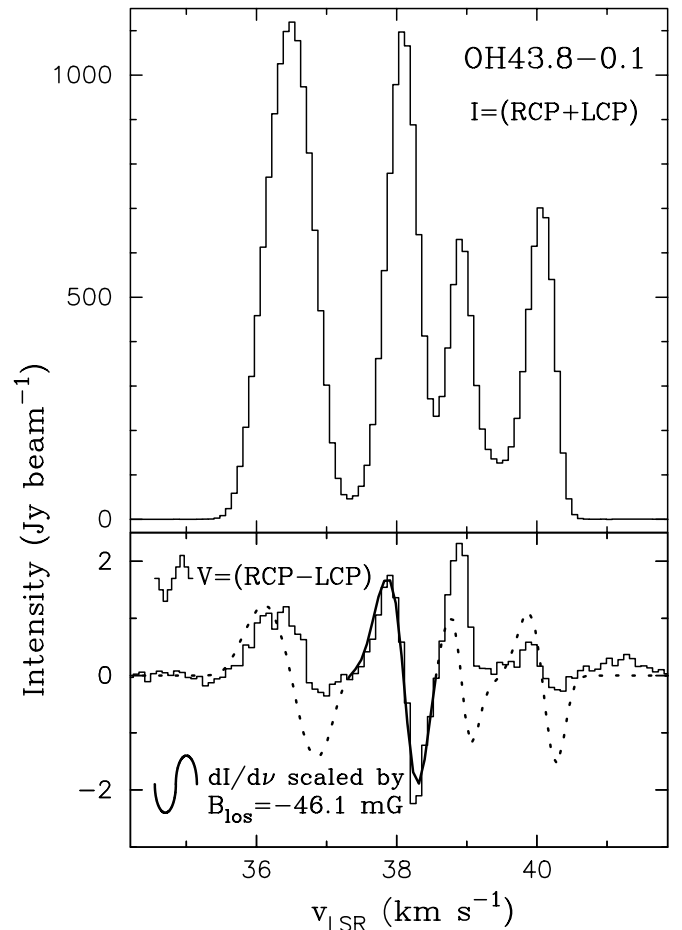


FIG. 5b

FIG. 5.—(a) Same as Fig. 2, but for the peak maser at position (0, 0) in OH 43.8–0.1. The superposed curve in the bottom panel is scaled by $B_{\text{los}} = -19.2 \pm 1.6$ mG. The solid portion of this curve represents the channels over which the fit was made. (b) Same as (a), except that the superposed curve is scaled by $B_{\text{los}} = -46.1 \pm 2.5$ mG.

two groups separated by about $4''$. Each group coincides (to within $1''$) with a UC H II region.

VLA observations of the H_2O masers in Cep A were made in order to detect the Zeeman effect. The strongest maser, at -9.9 km s^{-1} , was found to have a peak intensity of 9750 Jy. The Stokes V profiles in this data set exhibit a ~ 5 Jy spike near -10 km s^{-1} that is spread over about four or five velocity channels. It is unlikely that this is due to external interference; there are no unidentified spikes in any of the 1999 data, of which this is a part. It is also unlikely that this is the sidelobe of a maser that was not properly cleaned, since there are no obvious maser features narrow enough to produce such a narrow spike. Displays of the UV data in the relevant channels also do not reveal any overwhelmingly bad points. We ascribe the spike to some unidentified bad data and exclude the affected channels from the fits. This does prevent us from setting an upper limit on the Zeeman effect for the strongest maser. However, there is a maser in the northern group (of the two groups identified by Lada et al. 1981) that is not affected by these bad channels. Upper limits on the Zeeman effect were set for this maser. The line parameters and magnetic field values from the formal fits for this maser are given in Table 5.

5. DISCUSSION

5.1. Basic Discussion of Observational Results

The current observations represent the first comprehensive VLA study of the Zeeman effect in H_2O masers. If interpreted according to the formulation of Nedoluha & Watson (1992; also see § 3), these measurements imply B_{los} in the range from 13 to 49 mG in several high-mass star-forming regions (Table 4) and upper limits of 90 mG or less in some other regions (Table 5). These values are of the same order as the Fiebig & Güsten (1989) single-dish results. The only case in which a comparison can be attempted with their results is for the W3 IRS 5 region. However, Fiebig & Güsten (1989) observed this region with a $41''$ beam. Therefore, all three maser spots shown in Figure 1 would have appeared within their beam, making direct comparison with the VLA results difficult. Scaling of their result for the -40.5 km s^{-1} maser (using $z = 2.1 \text{ Hz mG}^{-1}$) gives $B_{\text{los}} = -28.7 \pm 8.7 \text{ mG}$. This is in good agreement with the value of -30 mG obtained from an intensity-weighted average of our three magnetic field detections in W3 IRS 5 from Table 4.

In two instances in the present observations, significant fields have been found at two or more locations in an observed region. These detections provide a high-resolution map of the magnetic field in these regions over arcsecond scales. In W49 N, the field is observed to reverse over a $1''.1$ (0.06 pc) scale. In W3 IRS 5, the field has the same direction over a $0''.5$ (0.005 pc) scale. Higher resolution VLBA maps will provide a better view of this variation on even smaller scales (see, e.g., Sarma, Troland, & Romney 2001).

5.2. Theoretical Models for the Masers

Water masers are believed to be collisionally pumped in warm (400 K) postshock gas (Elitzur et al. 1989); recently, Watson, Sarma, & Singleton (2002) have shown that strong 22 GHz H_2O masers can arise in gas with even higher temperatures ($\sim 2000 \text{ K}$). In high-mass star formation regions, these shocks likely arise in shells driven by outflows. If the

shocks are fast enough ($u_s > 30\text{--}40 \text{ km s}^{-1}$), the H_2 is fully dissociated. Such a shock is known as a J-type shock. Lower velocity shocks, known as C-type shocks, do not fully dissociate H_2 . It appears that conditions behind both J-type and C-type shocks are quite similar, as far as H_2O maser generation is concerned (Elitzur et al. 1989; Kaufman & Neufeld 1996), except that 22 GHz masing in J-type shocks originates in a narrow range of temperatures near 400 K , whereas it can occur at gas temperatures up to 3000 K in C-type shocks. Gas densities in the postshock maser regions are believed to be in the range $10^8\text{--}10^{10} \text{ cm}^{-3}$. Lower densities provide insufficient collisional pumping; higher densities quench the maser by thermalizing the level populations. Given this scenario, the Zeeman observations reported here probe the postshock magnetic field, where the field energy limits the shock-induced gas compression.

5.3. Comparison of Observations with Models

To explore the significance of our magnetic field results in a postshock environment, we use three simple equations. First, in the case of flux conservation, the shock amplifies the field in proportion to the density ρ , i.e.,

$$B_0/\rho_0 = B_1/\rho_1, \quad (2)$$

where the subscripts 0 and 1 refer to the preshock and postshock (in this case, maser) regions, respectively. Strictly speaking, B_0 and B_1 are the components of the field parallel to the face of the shock. Also, if the postshock field, rather than the thermal pressure, limits the rise in density, then the magnetic field energy density equals the shock ram pressure, or

$$B_1^2/8\pi = \rho_0 u_s^2, \quad (3)$$

where u_s is the shock velocity. Finally, the preshock field strength and gas density might obey the approximate empirical relation discussed by Crutcher (1999), i.e., $B_0 \propto n_0^{1/2}$. Crutcher's Figure 1 is a log-log plot of the line-of-sight magnetic field versus $n(\text{H}_2)$ from observational data for molecular clouds. We have evaluated the proportionality constant in the scaling relationship of his Figure 1, leading to the relation

$$B_0 = \beta \rho_0^{1/2}, \quad (4)$$

where $\beta \approx 5.8 \times 10^5$ in cgs units and where we have assumed on statistical grounds that B_0 is twice the line-of-sight magnetic field (see, e.g., Crutcher 1999). Equation (4), with a similar value of β , is also given by Heiles et al. (1993). Equations (2)–(4) contain four unknowns (ρ_0 , ρ_1 , u_s , and B_0), if we assume that the value of B_1 is determined by the H_2O maser Zeeman effect. Therefore, we can determine any three of these unknowns if we assume a value for the fourth. Furthermore, if we assume that u_s is known from derived maser space velocities (see below), then all other parameters are determined.

We have explored the parameter space of equations (2)–(4) in order to find reasonable values of all quantities. We first take an average value of 30 mG for B_{los} , based on the Zeeman detections (Table 4). Then we assume $B_1 = 2B_{\text{los}}$ and $B_1^2 = 3B_{\text{los}}^2$ on statistical grounds (see, e.g., Crutcher 1999). We find that values of $u_s > 20 \text{ km s}^{-1}$ yield $n_1(\text{H}_2) < 10^8 \text{ cm}^{-3}$, below the value required theoretically for efficient maser amplification. This criterion can be

relaxed by assuming that B_1 is a factor of 2 higher, in which case u_s can be as high as 60 km s^{-1} . However, there are several reasons for believing that this circumstance does not apply. First, the low center velocities of the masers in question (i.e., center velocities comparable to the molecular line velocities in the clouds) suggest that these masers are not associated with high-velocity J-shocks (also see Watson et al. 2002). Second, the space velocities of the masers derived by other authors from VLBI proper-motion studies are a good indicator of the shock velocities; a typical value of the shock velocity for W3 IRS 5 is about 20 km s^{-1} (Imai et al. 2000). Finally, the magnetic field strengths are unlikely to be significantly higher than the values we measure unless the field is tangled in the emitting region. However, maser emission regions are loci of velocity coherence, so significant tangling of the field seems unlikely. We conclude that a consistent model of the postshock maser region where we measure magnetic fields can be constructed satisfying equations (2)–(4). This model allows a postshock density that is high enough for efficient maser pumping (10^8 cm^{-3}), low C-shock velocities, as suggested by proper-motion data (20 km s^{-1}), and postshock magnetic field strengths consistent with the Zeeman effect data ($B_{\text{los}} = 30 \text{ mG}$). In such a model, the postshock gas density and field strength are each amplified by a factor of about 20, so the preshock density $n_0 \sim 5 \times 10^6 \text{ cm}^{-3}$, and the preshock magnetic field $B_0 \sim 3 \text{ mG}$. These conditions are very similar to those described by Güsten, Fiebig, & Uchida (1994) for dense, thermally excited gas bordering the W3(OH) compact H II region. These authors observed the Zeeman effect in a 13.4 GHz excited-state OH absorption line. They found $B_{\text{los}} = 3.1 \pm 0.4 \text{ mG}$ in gas with an estimated density of $7 \times 10^6 \text{ cm}^{-3}$. Dense molecular gas of this nature is a likely candidate for preshock conditions for H_2O masers. Also, gas in this density range characterizes the W49 N molecular studies by Serabyn, Güsten, & Schulz (1993).

An alternate possibility is that we have significantly *overestimated* the field strength by using the Nedoluha & Watson (1992) thermal approximation, rather than the formulation of Elitzur (1998; see § 3). In such a case, the actual field strength B_1 in the maser regions could easily be a factor of 4 less than we have assumed, depending on the angle of the field to the line of sight. However, if we assume such a low maser field, then the derived values of $n_1(\text{H}_2)$ are all less than 10^7 cm^{-3} , even for values of u_s as low as 20 km s^{-1} . We conclude that such an overestimate of the maser field is quite unlikely, unless the masers can operate efficiently at densities significantly lower than those predicted by the maser models. Evidently, the thermal approximation of Nedoluha & Watson (1992) yields the more accurate estimate of maser magnetic fields.

Indirect estimates of magnetic field strengths for the H_2O masers in W49 N have been recently reported by Liljeström & Gwinn (2000). Their estimates are based on an extensive series of single-dish and VLBI observations previously obtained by these authors and their collaborators (Liljeström et al. 1989; Gwinn et al. 1992). Liljeström & Gwinn (2000) estimate mean maser (i.e., postshock) field strengths using equation (3) (their eq. [5]). They take the mean space velocity of the masers measured from the VLBI data as the shock velocity, and they estimate the preshock density. For the “inside masers” of W49 N (those with radial velocities inside the range of the dense ambient gas, i.e., $v_{\text{LSR}} = -2$ to 18 km s^{-1}), they take $u_s = 38 \text{ km s}^{-1}$ and $n_0 = 7.5 \times 10^6$

cm^{-3} . Equation (3) then yields $B_1 = 80 \text{ mG}$. This estimate of the mean W49 N maser field strength can be compared with the Zeeman effect results from the present observations, which yield $B_1 \approx 2B_{\text{los}} = 35\text{--}45 \text{ mG}$ for W49 N (Table 4). Liljeström & Gwinn (2000) also estimate the maser (i.e., postshock) gas density from the preshock density and the shock speed (their eq. [11], a combination of our eqs. [2]–[4]). For the inside masers, they find a mean gas density of $4 \times 10^8 \text{ cm}^{-3}$. Evidently, the physical parameters estimated by these authors are comparable to those we have taken for the maser model described above.

5.4. Energetics in the Masing Regions

The observed values for the magnetic field can also be used to investigate the energetics in these masing regions. The magnetic energy density is given by $3B_{\text{los}}^2/8\pi$ (see § 5.3). For the average value of $B_{\text{los}} \approx 30 \text{ mG}$ (Table 4), the magnetic energy density is $1.1 \times 10^{-4} \text{ ergs cm}^{-3}$. The kinetic energy density is given by $(3/2)mn\sigma^2$, where $\sigma = \Delta v/(8 \ln 2)^{1/2}$ is the velocity dispersion, the mass $m = 2.8m_p$, and m_p is the proton mass. If $\Delta v = 0.6 \text{ km s}^{-1}$ (average value for Δv_{FWHM} from Table 4), the kinetic energy density is $4.6 \times 10^{-6} \text{ ergs cm}^{-3}$. This suggests that the magnetic energy is dominant in these clouds by an order of magnitude. However, masers occur only in special directions, along which they have developed the required velocity coherence. Hence, the actual line width in the clouds is probably larger than that traced by the masers. In fact, the kinetic energy density will be equal to the magnetic energy density if Δv_{FWHM} is increased by a factor of 5. Such an increase would give $\Delta v_{\text{FWHM}} = 3 \text{ km s}^{-1}$. This is a reasonable value for Δv_{FWHM} in GMCs (see, e.g., McKee 1999). Hence, the magnetic and kinetic energy densities are probably in equilibrium in the clouds where the masing action is taking place.

6. CONCLUSIONS

(1) Our VLA observations of the Zeeman effect in H_2O masers have yielded significant magnetic field detections in several high-mass star-forming regions. Upper limits have also been set on magnetic fields in some cases. The detected fields range from $B_{\text{los}} = 13$ to 49 mG , if we adopt the method of Nedoluha & Watson (1992).

(2) For some regions, the detected fields provide a 2–3 point sampling of the magnetic field, indicating the nature of field variations on arcsecond scales. In W3 IRS 5, the fields have the same direction over $0''.5$ and vary by a factor of ~ 3 . In W49 N, the detected fields appear to reverse over a scale of $1''.1$, but show almost the same magnitude.

(3) Comparing our observations with collisionally pumped models of H_2O masers in postshock gas, we construct a self-consistent model of the postshock maser region, in which the densities are high enough to allow efficient maser pumping (10^8 cm^{-3}), velocities are suggestive of C-shocks (20 km s^{-1}), and magnetic field strengths match the observed Zeeman effect values ($B_{\text{los}} = 30 \text{ mG}$). Moreover, the projected preshock magnetic fields and densities agree well with values of the magnetic field and densities in locales that are likely candidates for the preshock regions of water masers.

(4) The formulation of Elitzur (1998) suggests that we have significantly overestimated the field strength. How-

ever, scaling our observed field values down by even a factor of 4 gives derived values of the density that are much lower than the values required by theoretical models for efficient maser operation. Hence, such an overestimate of the field by us is quite unlikely, unless H₂O masers can operate efficiently at densities significantly lower than those predicted by maser models. Moreover, Elitzur's treatment of maser polarization did not consider the case of hyperfine splitting, which is applicable to H₂O masers. Hence, the Elitzur formulation might not apply to our observations anyway.

(5) Based on the observed values of the magnetic field, we find that the magnetic and kinetic energy densities in the maser regions will be in equilibrium if the line widths are of the order of 3 km s⁻¹. Since this is a reasonable value for the line width in molecular clouds, the magnetic field and kinetic energy densities are probably close to equilibrium.

(6) The importance of H₂O masers has been established, not only as unique tracers of the Zeeman effect in high-density regions, but also as probes of the magnetic field in shocked regions. Future directions include higher resolution

observations of the Zeeman effect and longer observation times to increase the sensitivity of detection, in order to obtain magnetic field measurements at many more positions in the cloud.

The authors would like to thank Moshe Elitzur and W. D. Watson for helpful and stimulating discussions and an anonymous referee for comments that have helped to improve the manuscript. A. P. S. wishes to thank John Connolly for making available a Center for Computational Sciences fellowship and for computational support. This work has also been partially supported by NSF grants AST 98-20641 and AST 99-88341. A. P. S. extends his thanks to Barry Clark for making available one hour of ad hoc VLA time a week before each of the two observations; these two hours were of immense help and allowed A. P. S. to finalize the list of masers to observe for the Zeeman effect. These observations formed part of the doctoral thesis of A. P. S. at the University of Kentucky.

REFERENCES

- Alcolea, J., Menten, K. M., Moran, J. M., & Reid, M. J. 1993, in *Astrophysical Masers*, ed. A. W. Clegg & G. E. Nedoluha (Berlin: Springer), 225
- Benson, J. M., & Johnston, K. J. 1984, *ApJ*, 277, 181
- Blaauw, A., Hiltner, W. A., & Johnson, H. L. 1959, *ApJ*, 130, 69
- Caswell, J. L., & Reynolds, J. E. 2001, *MNRAS*, 325, 1346
- Claussen, M. J., Gaume, R. A., Johnston, K. J., & Wilson, T. L. 1994, *ApJ*, 424, L41
- Claussen, M. J., et al. 1984, *ApJ*, 285, L79
- Crutcher, R. M. 1999, *ApJ*, 520, 706
- Crutcher, R. M., Troland, T. H., Goodman, A. A., Heiles, C., Kazès, I., & Myers, P. C. 1993, *ApJ*, 407, 175
- De Pree, C. G., Wilner, D. J., Goss, W. M., Welch, W. J., & McGrath, E. 2000, *ApJ*, 540, 308
- Downes, D., Genzel, R., Moran, J. M., Johnston, K. J., Matveenko, L. I., Kogan, L. R., Kostenko, V. I., & Rönnäng, B. 1979, *A&A*, 79, 233
- Dreher, J. W., Johnston, K. J., Welch, W. J., & Walker, R. C. 1984, *ApJ*, 283, 632
- Dreher, J. W., & Welch, W. J. 1981, *ApJ*, 245, 857
- Elitzur, M. 1992, *ARA&A*, 30, 75
- . 1996, *ApJ*, 457, 415
- . 1998, *ApJ*, 504, 390
- Elitzur, M., Hollenbach, D. J., & McKee, C. F. 1989, *ApJ*, 346, 983
- Elmegreen, B. G., Genzel, R., Moran, J. M., Reid, M. J., & Walker, R. C. 1980, *ApJ*, 241, 1007
- Fiebig, D., & Güsten, R. 1989, *A&A*, 214, 333
- Forster, J. R., Welch, W. J., & Wright, M. C. H. 1977, *ApJ*, 215, L121
- Genzel, R., et al. 1978, *A&A*, 66, 13
- Georgelin, Y. M., & Georgelin, Y. P. 1976, *A&A*, 49, 57
- Güsten, R., Fiebig, D., & Uchida, K. I. 1994, *A&A*, 286, L51
- Gwinn, C. R., Moran, J. M., & Reid, M. J. 1992, *ApJ*, 393, 149
- Heiles, C., Goodman, A. A., McKee, C. F., & Zweibel, E. G. 1993, in *Protostars and Planets III*, ed. E. H. Levy & J. I. Lunine (Tucson: Univ. Arizona Press), 279
- Humphreys, R. M. 1978, *ApJS*, 38, 309
- Imai, H., Deguchi, S., & Sasao, T. 2002, *ApJ*, 567, 971
- Imai, H., Kameya, O., Sasao, T., Miyoshi, M., Deguchi, S., Horiuchi, S., & Asaki, Y. 2000, *ApJ*, 538, 751
- Kaufman, M. J., & Neufeld, D. A. 1996, *ApJ*, 456, 250
- Lada, C. J., Blitz, L., Reid, M. J., & Moran, J. M. 1981, *ApJ*, 243, 769
- Liljeström, T., & Gwinn, C. R. 2000, *ApJ*, 534, 781
- Liljeström, T., Mattila, K., Toriseva, M., & Anttila, R. 1989, *A&AS*, 79, 19
- Matthews, H. E., Shaver, P. A., Goss, W. M., & Habing, H. J. 1978, *A&A*, 63, 307
- McKee, C. F. 1999, in *The Origin of Stars and Planetary Systems*, ed. C. J. Lada & N. D. Kylafis (Dordrecht: Kluwer), 29
- Moran, J. M., et al. 1973, *ApJ*, 185, 535
- Morris, M. 1976, *ApJ*, 210, 100
- Nedoluha, G. E., & Watson, W. D. 1991, *ApJ*, 367, L63
- . 1992, *ApJ*, 384, 185
- Reid, M. J., Argon, A. L., Masson, C. R., Menten, K. M., & Moran, J. M. 1995, *ApJ*, 443, 238
- Reid, M. J., Haschick, A. D., Burke, B. F., Moran, J. M., Johnston, K. J., & Swenson, G. W., Jr. 1980, *ApJ*, 239, 89
- Rodríguez, L. F., Moran, J. M., Ho, P. T. P., & Gottlieb, E. W. 1980, *ApJ*, 235, 845
- Sargent, A. I. 1977, *ApJ*, 218, 736
- Sarma, A. P., Troland, T. H., & Romney, J. D. 2001, *ApJ*, 554, L217
- Sault, R. J., Killeen, N. E. B., Zmuidzinas, J., & Loushin, R. 1990, *ApJS*, 74, 437
- Scoville, N. Z., Solomon, P. M., & Penzias, A. A. 1975, *ApJ*, 201, 352
- Serabyn, E., Güsten, R., & Schulz, A. 1993, *ApJ*, 413, 571
- Tieftunk, A. R., Gaume, R. A., Claussen, M. J., Wilson, T. L., & Johnston, K. J. 1997, *A&A*, 318, 931
- Troland, T. H., & Heiles, C. 1982, *ApJ*, 252, 179
- Turner, J. L., & Welch, W. J. 1984, *ApJ*, 287, L81
- Walker, R. C., Matsakis, D. N., & García-Barreto, J. A. 1982, *ApJ*, 255, 128
- Watson, W. D., Sarma, A. P., & Singleton, M. S. 2002, *ApJ*, 570, L37
- Watson, W. D., & Wyld, H. W. 2001, *ApJ*, 558, L55
- Wynn-Williams, C. G., Becklin, E. E., & Neugebauer, G. 1972, *MNRAS*, 160, 1
- Wyrowski, F., Hofner, P., Schilke, P., Walmsley, C. M., Wilner, D. J., & Wink, J. E. 1997, *A&A*, 320, L17